Interdash Coupling within Dense Ensembles of Quantum Dashes: Comparison of InAs/(In,Al,Ga)As/InP and InAs/(In,Al)As/InP Systems

P. Holewa[1,*] M. Gawełczyk[2,3,†] A. Maryński[1,‡] K. Ryczko[1] V. Liverini,[4,§] M. Beck[4] J. Faist[4] G. Sęk[1] and M. Syperek[1]

[1]*Laboratory for Optical Spectroscopy of Nanostructures, Department of Experimental Physics, Faculty of Fundamental Problems of Technology, Wrocław University of Science and Technology, Wybrzeże Wyspiańskiego 27, Wrocław 50-370, Poland*
[2]*Department of Theoretical Physics, Wrocław University of Science and Technology, Wrocław 50-370, Poland*
[3]*Institute of Physics, Faculty of Physics, Astronomy and Informatics, Nicolaus Copernicus University in Toruń, Grudziądzka 5, Toruń 87-100, Poland*
[4]*Institute of Quantum Electronics, ETH Zürich, Wolfgang-Pauli-Strasse 16, Zürich 8093, Switzerland*

Lasers, light-emitting diodes, and other optoelectronic devices employing InAs/InP quantum dots (QDs) instead of quantum wells (QWs) as their active parts benefit from the quasi-zero-dimensional (0D) density of states while maintaining the emission at the communication-relevant range of 1.55 μm. However, for certain application purposes, the substitution of QWs with QDs is advantageous only if QDs can either be treated as isolated objects or exhibit quantum-mechanical coupling between deeply confined states. Here, we compare two material systems of InAs/(In,Al,Ga)As/InP and InAs/(In,Al)As/InP elongated QDs (quantum dashes, QDashes) of comparable surface densities and interdash distances. We investigate the presence and type of coupling between QDashes, focusing on the direct tunnel coupling for both types of carriers manifested already at low temperature. In the time-resolved photoluminescence (PL) experiment, we observe a significant dispersion of the PL decay time for InAs/(In,Al,Ga)As QDashes, resulting from the migration of carriers from high- to low-energy QDashes due to substantial tunnel coupling. In the case of InAs/(In,Al)As QDashes, the dispersionless time dependence points toward the absence of such coupling. We confirm this interpretation with multiband $\mathbf{k \cdot p}$ calculations. We check that the proposed coupling scenario is possible and show its much higher probability for InAs/(In,Al,Ga)As than for InAs/(In,Al)As QDashes. Finally, in temperature-dependent PL, we observe the redistribution of holes among QDashes via thermal excitation to wetting-layer states for both systems, constituting an additional interdash coupling channel at elevated temperatures. Our results indicate that the InAs/(In,Al)As QDash system is preferential for optoelectronic applications where QD isolation is highly sought after, whereas InAs/(In,Al,Ga)As QDashes exhibit quantum-mechanical coupling between deeply confined states.

I. INTRODUCTION

Semiconductor InAs quantum dots (QDs) grown on the conventional InP(001) substrate have been actively studied in recent years as prospective light emitters for the telecommunication-relevant spectral range centered near 1.55 μm. The considered applications of these dots range from nonclassical single-photon emitters for quantum photonic circuits and quantum-secured optical data transmission lines [1–10] through a gain medium in lasers and optical amplifiers for classical mid- and long-haul optical-fiber networks [11–13] to more sophisticated applications, e.g., quantum cascade lasers [14–17] or light detectors [18]. These application prospects stem from the quasi-zero-dimensional (0D), atomic-like density of states in a QD and relatively strong quantum confinement.

On the one hand, the standard Stranski-Krastanov (SK) growth technique of InAs islands on InP allows one to obtain high areal density of these objects reaching 10^{10} - 10^{11} cm^{-2}, which is beneficial for lasers, amplifiers, or detectors. On the other hand, the relatively small lattice mismatch of approximately 3% between InAs and InP, and the SK growth kinetics of the islands on InP substrate can lead to their substantial elongation along the [1$\bar{1}$0] crystallographic direction. It additionally results in their

* pawel.holewa@pwr.edu.pl
† michal.gawelczyk@pwr.edu.pl
‡ Currently at McKinsey Knowledge Center Poland, 50-141 Wrocław, Poland
§ Currently at Albis Optoelectronics AG, 8803 Rüschlikon, Switzerland

broad size distribution. The length-to-width (L/W) aspect ratio for the InAs material island typically exceeds 2. Therefore, these structures are commonly called quantum dashes (QDashes).

The InAs QDashes are often embedded in barriers lattice matched to InP: (In,Al,Ga)As [11] or (In,Al)As [19], providing relatively strong carrier confinement due to reasonably deep confinement energy: ~240 meV for electrons and ~110 meV for holes, and ~500 meV and ~190 meV - for (In,Al,Ga)As and (In,Al)As, respectively. As discussed in detail in Sec. III C, the InAs QDashes providing relatively strong confinement and preventing the exchange of As and P atoms during the epitaxial growth. The InAs/(In,Al,Ga)As/InP(001) and InAs/(In,Al)As/InP(001) QDashes have been extensively studied concerning their band structure [20–22], polarization of emission [23], carrier and spin dynamics [24–28], and carrier confinement regime [27,29]. Nevertheless, there is still an open question on the extent to which QDashes can be treated as isolated objects within their dense ensembles.

The answer is crucial for target-specific applications that rely on a high-density QDash matrix. For classical QD or QDash lasers, the lateral coupling between deeply confined states of adjacent emitters raises doubts on preserving truly 0D carrier confinement that is beneficial for the operation of the laser [30]. Such coupling can potentially open a new carrier escape channel, affecting the spectral gain, the emission wavelength, and the temperature stability of the device parameters. However, the same coupling can be beneficial by lowering the threshold current density, improving the internal efficiency, and narrowing the laser gain, which has been shown for laser devices with vertically [31] and laterally coupled QDs [30] even at room temperature [32]—provided that defect-assisted nonradiative losses due to barrier states are not introduced [33]. The coupling is also an underlying operation principle of recently proposed ultranarrow-line superradiant nanolasers [34,35]. In contrast to classical QD and QDash lasers, the presence of coupling is not acceptable for superluminescent light-emitting diodes, as it narrows the spectral bandwidth [36]; however, it is indispensable for the operation of QD- or QDash-based quantum cascade lasers [37]. In the case of QD-based detectors, the coupling can increase the dark current, causing the overall performance of the device to deteriorate [18]. Therefore, the presence or absence of direct electronic coupling between QDs or QDashes stands as a vital issue for device performance and may cause the overall performance to deteriorate or, conversely, may enable the operation of a device, depending on the specific application.

Within the QDash ensembles, three coupling schemes are possible [38]: (i) direct coupling involving the tunneling of carriers between ground states or between ground and excited states of adjacent QDashes; (ii) coupling via higher discrete states (DSs); or (iii) coupling via higher continuum states (CS). The DS may have different origins involving, e.g., 0D wetting-layer (WL) states induced by fluctuations in the WL width or chemical composition (so-called natural QDs), structural defects forming a band tail energetically located below the WL mobility edge [39,40], hybrid QD-WL states [41–46], or high-energy 0D QD states. In the latter case, the states can be spatially extended and in dense ensembles of nanostructures form minibands [47,48], remotely resembling a superlattice. These mechanisms of carrier exchange differ in some aspects. First, they involve different ranges of carrier energy changes, which becomes apparent in the different temperature ranges. Direct coupling is already present at low temperature. In contrast, coupling via DSs requires the promotion of carriers to the DSs, sometimes via the excited states ladder, which are delocalized [38]. For the carrier redistribution via excitation to the continuum of two-dimensional (2D) WL states, even higher temperatures are needed. Second, the requirements of a dash-to-dash distance vary: the efficiency of the direct tunneling drops more significantly with the distance [49] than the coupling through higher states (DSs and CSs). In the case of DSs, carriers are less confined in QDashes than in their ground states, so their wave functions are more spread, which extends the range of coupling [50]. Finally, coupling via the 2D WL states can also be present in low-density structures with large dash-to-dash distances, as it involves the movement of carriers in the WL plane [51].

Direct coupling has been observed for pairs of epitaxial QDs in vertically arranged QD stacks [52,53] or in laterally coupled QDs, so-called QD molecules [54–56], as well as in QD chains [57,58]. Although the coupling between InAs QDashes grown directly on InP(001) has been investigated experimentally, with indications of transfer via discrete and WL states [59], only theoretical considerations on the direct-coupling mechanism [60] are available, lacking experimental confirmation.

In this work, we study interdash coupling scenarios in two telecom-application-relevant InAs/(In,Al,Ga)As/ (001)InP and InAs/(In,Al)As/(001)InP QDash ensembles of high areal density employing time-resolved photoluminescence (TRPL) and time-integrated PL supported by other spectroscopic methods: photoluminescence excitation (PLE) and photoreflectance ($\Delta R/R$). We show that at elevated temperatures, both QDash systems exhibit the presence of WL-mediated CS coupling. More importantly, with low-temperature TRPL studies, we show the manifestation of direct interdash coupling for InAs/(In,Al,Ga)As QDashes. In this case, we interpret the coupling as carrier tunneling from the ground state in a QDash of high emission energy into excited states of a QDash with a lower emission energy. Subsequently, carriers relax to the ground state, form an exciton, and recombine. Additionally, we realistically model both types of QDashes and use multiband $\mathbf{k \cdot p}$ calculations to evaluate the likelihood

of this coupling scenario. On the contrary, for the InAs/(In,Al)As QDashes, we observe no indications of direct coupling in TRPL, which makes the system more interesting for applications in optoelectronics due to its robust emitter isolation.

II. EXPERIMENTAL AND THEORETICAL METHODOLOGY

In this section, we give details of epitaxial growth, optical experiments, and the theoretical framework.

A. Epitaxial growth

Both types of InAs QDashes are grown in a molecular-beam-epitaxy reactor on an InP:Fe(001) semi-insulating substrate. Their growth is similar to that described in Ref. [16] (for InAs/$In_{0.53}Ga_{0.23}Al_{0.24}$As/InP) and in Ref. [17] (for InAs/$In_{0.52}Al_{0.48}$As/InP). For both systems, we use an As_2 source and the growth sequence starts with the deposition of a 400-nm-thick buffer of the barrier material [(In,Al)As or (In,Al,Ga)As] on top of the InP substrate, followed by nominally 6 monolayers (MLs) of InAs, capped by 100-nm-thick barrier material. The growth sequence is finished with an uncapped InAs QDash layer, grown under the same conditions as the buried ones for scanning-electron-microscopy (SEM) investigation. The samples differ in their V:III ratio and in the growth temperature applied during the QDash growth: for InAs/(In,Al,Ga)As, these parameters are 22 and 480 °C, while for InAs/(In,Al)As we have 32 and 490 °C, respectively.

B. Optical experiments

For the optical experiments, the structures are kept in a helium-flow cryostat with temperature control in the range of 5–300 K. In the case of time-integrated PL experiments in a nonresonant pumping scheme, a continuous-wave (cw) laser line at $E_{exc} = 1.94$ eV is employed, focused to the laser spot diameter of approximately 140 μm. For nonresonant excitation and TRPL experiments, the structures are excited with $E_{exc} = 1.54$ eV photon energy by trains of 50-ps pulses with a 40-MHz repetition frequency, focused to the spot diameter of approximately 5 μm, provided by a pulsed laser diode. For both experiments, emitted photons are collected by a lens system and spectrally dispersed in a 0.3-m-focal-length monochromator with two outputs. One of the outputs is equipped with a single-channel InAs detector measuring the time-integrated PL with the lock-in technique. At the second output, photons are directed to an optical fiber and sent to a superconducting NbN single-photon detector for the TRPL measurement with the time-correlated single-photon-counting technique. We estimate the overall time resolution of the setup used for

the TRPL studies to be $\tau_S \approx 80$ ps. The PLE experiment is performed using the same optical setup and the PLE intensity is examined at the detection energy set to the center of the peak while scanning the excitation energy. In this case, the structures are excited by a train of roughly 2-ps-long pulses coming from the optical parametric oscillator (OPO), which is synchronously pumped by a Ti:sapphire oscillator operating at 76-MHz repetition frequency. The photon energy in the pulse is tuned in a broad range of 0.86–1.1 eV. The OPO pulse source is also employed for the quasiresonant excitation in PL and in the TRPL experiments. Within this scheme, the OPO energy is tuned to approximately 20 meV and approximately 34 meV above the high-energy edge of the PL spectrum for InAs/(In,Al)As and InAs/(In,Al,Ga)As QDashes, respectively. Additionally, for the temperature-dependent experiments, the laser line is red shifted according to the expected Varshni trend to account for the thermal shift of the band structure.

The $\Delta R/R$ experiment is performed in the PL setup. The energy-band structure is perturbed at a carrier frequency of $f_{mod} = 250$ Hz by the cw laser beam at $E_{exc} = 1.94$ eV photon energy. The white light from a halogen lamp reflected off the sample is analyzed in the monochromator and detected by the InAs single-channel detector using the lock-in technique.

C. Theoretical framework

The modeling of the WL electronic structure (single-particle states) is performed with the commercially available NEXTNANO software [61]. For calculation of the QDash and double-QDash states, we use a state-of-the art implementation [62] of multiband $\boldsymbol{k} \cdot \boldsymbol{p}$ theory. The eight-band (conduction, heavy-, light-, and spin-orbit split-off hole bands) Hamiltonian (the explicit form is given in Ref. [63]) is discretized on an axis-wise regular grid. The nanostructures are modeled via position-dependent values of the material parameters. Diagonalization of the resultant matrix yields electron and hole eigenstates in the form of eight-component pseudospinors of discretized envelope functions, as well as their energies. The calculation includes the structural strain obtained within the continuum elasticity model by minimizing the elastic energy (the Dirichlet boundary condition for the vanishing of strain; $120 \times 100 \times 60$ nm^3 calculation domain), the strain-induced piezoelectric field with terms up to second order in strain components, as well as spin-orbit effects. Hamiltonian diagonalization is performed on a subdomain found by converging the results, with the Dirichlet boundary condition for a vanishing wave function. The relevant material parameters are taken from Ref. [64]. Our approach does not take into account the Coulomb interaction between carriers. However, it is sufficient to

TABLE I. The structural parameters of the QDash ensembles: MV, median value; σ, standard deviation.

Parameter		InAs/(In,Al,Ga)As	InAs/(In,Al)As
Surface density		7×10^{10} cm^{-2}	10^{11} cm^{-2}
Height H		2.4 ± 0.5 nm	
Distance d	MV	9 nm	12.5 nm
	σ	2.7 nm	3.8 nm
Width W	MV	15 nm	16 nm
	σ	4.6 nm	5.8 nm

determine the band structure, calculate the WL energy levels, and estimate the average dimensions of the QDashes that contribute to the PL peak.

III. EXPERIMENTAL RESULTS AND DISCUSSION

In this section, we present the analysis of the QDash geometry and the results of the comparative optical studies of both structures. Moreover, we show the analysis of the temperature-driven changes in the PL spectra supported with the results from the WL and QDash electronic-band-structure calculation realized in the eight-band $\mathbf{k} \cdot \mathbf{p}$ framework. Finally, we show and discuss the dispersion of the PL decay and rise times.

A. Structural data and analysis

Figure 1 presents SEM images of QDashes grown on the surface of the structure. They show high and comparable QDash areal densities: 7×10^{10} cm^{-2} for InAs/(In,Al,Ga)As [Fig. 1(a)] and 10^{11} cm^{-2} for InAs/(In,Al)As [Fig. 1(b)]. We assume that the geometry of optically active buried QDashes studied in the optical experiments is similar to that of the surface ones. The SEM-image analysis provides averaged QDash parameters, summarized in Table I (the interdash distance d and QDash width W). The QDash height H is determined based on transmission electron microscopy (TEM) [17,65]. The dash length is widely distributed in the range of 25–200 nm for InAs/(In,Al)As QDashes and 25–300 nm for InAs/(In,Al,Ga)As QDashes, with median values of approximately 40 nm and approximately 50 nm, respectively. The interdash distance, presented in Fig. 1(c), is defined as the distance between neighboring QDashes, measured at 50% of their height. This definition allows for the most accurate determination of the W and d from SEM images. The distributions of d cover similar ranges for both QDash ensembles so that the interdash distance is comparable between both structures. Note that in both ensembles, QDashes with $d \leq 6$ nm can be found.

B. Optical emission and absorption spectra

The normalized PL spectra from ensembles of QDashes taken at $T = 12$ K are presented in Fig. 2(a). Both PL
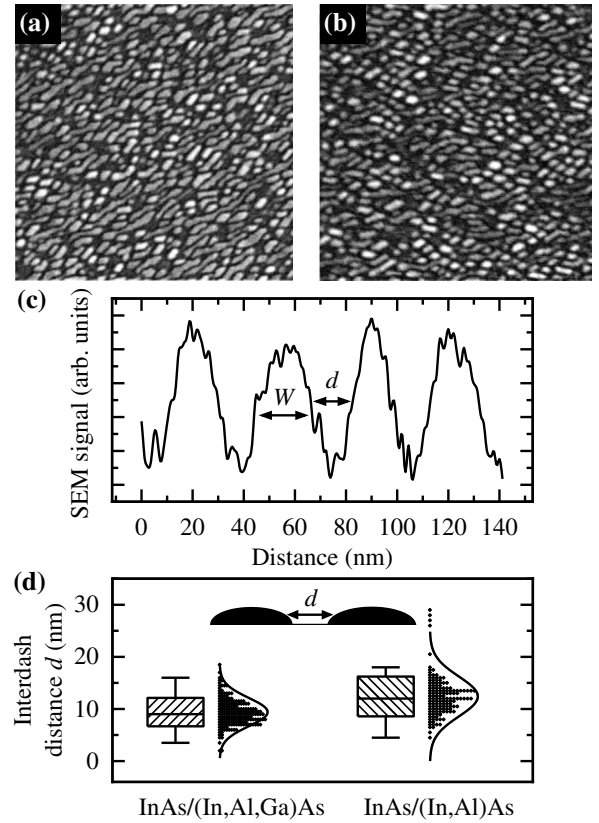
FIG. 1. The 800×800 nm^2 scanning-electron-microscopy (SEM) images of the investigated structures: (a) InAs/(In,Al,Ga)As and (b) InAs/(In,Al)As QDashes. (c) An exemplary cross section of the SEM image taken along the direction perpendicular to the elongation of four adjacent QDashes. The signal maxima correspond to QDashes. The QDash width (W) and interdash distance (d) are determined for each QDash locally at 50% of the QDash height. (d) The distributions of interdash distance d for InAs/(In,Al,Ga)As and InAs/(In,Al)As QDashes. The boxes mark the one-standard-deviation range, while the whiskers define the outliers ($1.5\times$ the standard deviation). The curves are normal-distribution profiles fitted to the histograms. The inset shows a schematic cross section of two adjacent semiellipsoid QDashes.

bands share the emission energy range, between roughly 0.76 eV and 0.83 eV. However, the spectral broadening for InAs/(In,Al)As QDashes (approximately 55 meV) is twice as large as for the InAs/(In,Al,Ga)As QDashes (approximately 27 meV) and, as a result, the emission range for the former extends up to approximately 0.9 eV. Commonly, the spectral broadening originates from inhomogeneities of size, shape, and chemical composition in the ensemble. We also check the evolution of the spectra under varying excitation power to confirm that the observed emission peak is related to the recombination of excitons in their QDash ground states. Figures 2(c) and
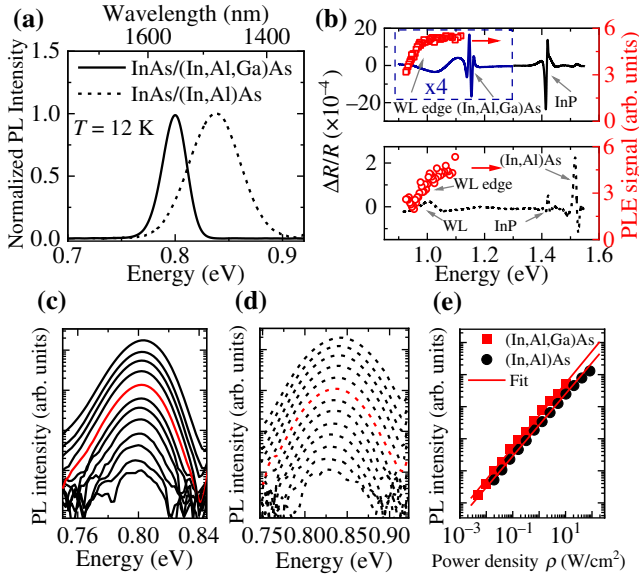
FIG. 2. (a) Normalized PL spectra taken at $T = 12$ K for InAs/(In,Al,Ga)As (solid line) and InAs/(In,Al)As (dashed line) QDashes. (b) The photoreflectance ($\Delta R/R$, lines) and photoluminescence excitation (PLE, points) signals for InAs/(In,Al,Ga)As (top) and InAs/(In,Al)As (bottom) QDashes. PLE is taken at 0.8 eV and 0.84 eV emission energy, respectively, at $T = 5$ K. (c),(d) Power-dependent PL spectra for (c) InAs/(In,Al,Ga)As and (d) InAs/(In,Al)As QDashes, taken at $T = 12$ K. The red lines mark the spectra taken at the same excitation power as used for the temperature-dependent PL investigations. (e) The integrated PL intensity for the spectra in panels (c) and (d), with power-law fits.

2(d) present the PL spectra for both QDash ensembles, with the excitation power varying by 4 orders of magnitude. No additional high-energy peaks emerge even at high excitation power, which can be traced back to the very high excitation power needed to fill the ground states of QDashes due to their high surface density. We plot the PL intensity I versus the excitation power P dependencies in Fig. 2(e) and we fit them with the power function $I(P) =$

aI^b. The exponents obtained prove the linear behavior, with values of $b = 1.001 \pm 0.017$ and $b = 0.971 \pm 0.014$ for InAs/(In,Al,Ga)As and InAs/(In,Al)As QDashes, respectively. Notably, the temperature-dependent and time-resolved PL studies are conducted in the regime of low excitation power to focus on the QDash ground-state properties.

Before discussing the carrier redistribution processes and carrier coupling schemes between QDashes, we need to establish information on the relevant energy scales that define the carrier confinement in the structures. Figure 2(b) shows the $\Delta R/R$ traces combined with the PLE signal intensity for the structures in question. The $\Delta R/R$ traces show spectral features at energies corresponding to the absorption edges of (In,Al)As (approximately 1.523 eV) and (In,Al,Ga)As (approximately 1.150 eV) barriers and the InP substrate (approximately 1.418 eV), in agreement with previous reports for similar structures [20,21]. Moreover, the $\Delta R/R$ signal for InAs/(In,Al)As QDashes shows a feature at approximately 1.03 eV, which overlaps with the absorption edge identified in the PLE spectrum. We attribute it to the optical transition in the WL. The WL-related optical transition for the InAs/(In,Al,Ga)As structure is clearly revealed only in the PLE spectrum at approximately 1.0 eV (which is consistent with other reports [21]), while in the $\Delta R/R$ trace, only a slight modulation is observable. The average energy distance between the PL peak of QDash emission and the WL absorption edge ($\Delta E_{\mathrm{QDash-WL}}$) is similar for both structures and reaches roughly 200 meV. However, the energy difference between the barrier and the WL absorption edge ($\Delta E_{\mathrm{WL-barrier}}$) is more than three times larger for the structure with the (In,Al)As barrier than for the one with (In,Al,Ga)As. All the derived parameters are summarized in Table II.

C. Temperature-dependent photoluminescence

The temperature-induced changes in the PL spectra for the two examined structures are compared in Fig. 3. A correlation can be observed in the integrated PL intensity

TABLE II. The characteristic energies for both material systems determined from the PL, PLE, and $\Delta R/R$ traces ("Experiment") and calculated within the eight-band $\boldsymbol{k \cdot p}$ approach ("Calculations"): E_{WL}, the energy of the wetting-layer (WL) absorption edge; E_{QDash}, the energy of the PL peak center of mass for QDashes. $\Delta E_{\mathrm{QDash-WL}} = E_{\mathrm{WL}} - E_{\mathrm{QDash}}$, $\Delta E_{\mathrm{WL-barrier}} = E_{\mathrm{barrier}} - E_{\mathrm{WL}}$.

| | InAs/(In,Al,Ga)As QDash system | | InAs/(In,Al)As QDash system | |
	Experiment	Calculations	Experiment	Calculations
E_{QDash}	~ 0.80 eV	0.809 eV	~ 0.84 eV	0.848 eV
E_{WL}	~ 1.00 eV	0.984 eV	~ 1.03 eV	1.020 eV
E_{barrier}	~ 1.150 eV	1.154 eV[a]	~ 1.523 eV	1.528 eV[a]
$E_{\mathrm{substrate}}$	~ 1.418 eV	1.423 eV[a]	~ 1.418 eV	1.423 eV[a]
$\Delta E_{\mathrm{QDash-WL}}$	~ 200 meV	175 meV	~ 190 meV	172 meV
$\Delta E_{\mathrm{WL-barrier}}$	~ 150 meV	170 meV	~ 493 meV	508 meV

[a]Derived directly from literature parameters [64].

(top row), the peak energy (center), and the spectral broadening of the emission peak (bottom). The time-integrated spectra are recorded under a constant laser-power density of approximately 0.65 W/cm^2 for InAs/(In,Al,Ga)As and approximately 2.6 W/cm^2 for InAs/(In,Al)As QDashes, which is in the low-power excitation limit for both ensembles [see Fig. 2(e)]. We note that the PL emission for InAs/(In,Al,Ga)As QDashes can be tracked up to approximately 130 K for nonresonant excitation and up to approximately 100 K for the quasiresonant one. On the contrary, the emission from the InAs/(In,Al)As QDashes is observed up to nearly room temperature under the nonresonant excitation case and up to approximately 240 K for the quasiresonant one. These results may be explained by the stronger carrier confinement in InAs/(In,Al)As QDashes, as already stated in Table II. Carriers excited from QDashes to the WL can most likely be redistributed back between them without much loss among the WL states. Although the WL for the InAs/(In,Al,Ga)As QDashes is at a similar energy distance from the QDash ground state as for the InAs/(In,Al)As QDashes, the energy distance from the WL to the barrier is much smaller, allowing for the depletion of the WL reservoir through barrier states. Interestingly, for the InAs/(In,Al)As QDashes, we observe a qualitatively different dependence of the PL intensity on the temperature for non- and quasiresonant excitation. We attribute the slight increase of the PL intensity under nonresonant excitation to thermal activation of carriers from shallow traps (in the WL or in the barrier), effectively providing additional carriers to QDashes. Therefore, in this case, the interpretation of the temperature-dependent PL evolution is more complex, so we also analyze the results obtained under quasiresonant excitation. In this excitation scheme, the carriers are injected directly into QDash excited states and, as a result, no increase of the PL intensity at elevated temperatures is observed [see Fig. 3(d)].

To identify the most efficient carrier-excitation channels, the temperature-dependent PL intensity is fitted with a standard formula assuming two activation processes [66]:

$$I(T) = \frac{I_0}{1 + B_1 \exp(-E_{a,1}/k_B T) + B_2 \exp(-E_{a,2}/k_B T)},$$

(1)

where I_0 is the PL intensity for $T \to 0$, $E_{a,1}$ and $E_{a,2}$ are activation energies, and B_1 and B_2 are relative rates corresponding to the efficiency of the processes involved.

The fitting curves are displayed as solid red lines in Figs. 3(a) and 3(d), and the relevant PL quenching parameters are summarized in Table III. To interpret the quenching energies, we calculate the energy levels within the eight-band $\mathbf{k \cdot p}$ approach. First, we calculate the electron and hole ground-state energies in the WL as a function of its thickness. For simplicity, we assume the WL to be pure
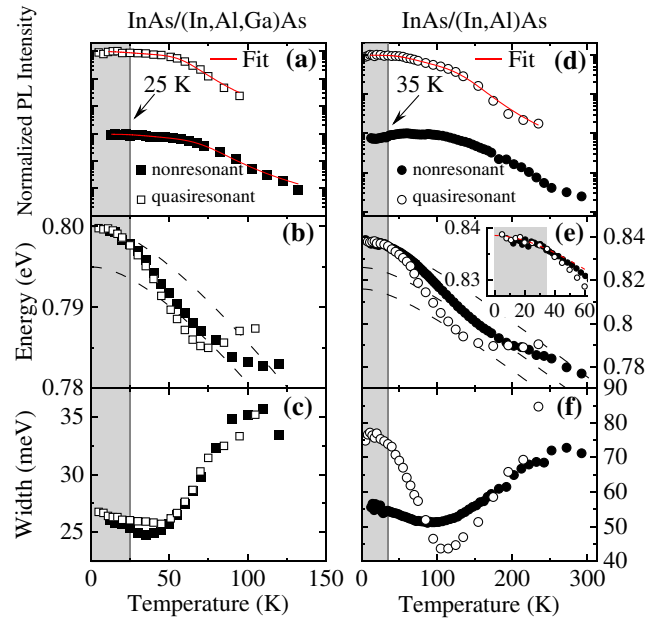
FIG. 3. The temperature dependence of PL emission from InAs/(In,Al,Ga)As (left-hand panel) and InAs/(In,Al)As (right-hand panel) QDashes. Top, the normalized PL intensity under nonresonant (full symbols) and quasiresonant (open symbols) pumping with fitted Arrhenius curves. The points and curves are shifted vertically for clarity. Center, the thermal shift of the PL peak emission energy (points) with Varshni trends (dashed lines). Bottom, the temperature-dependent width of the PL peak. The inset in (e) shows an enlargement of data for the low-temperature range. The shaded areas mark the low-temperature range as defined in the text. The experiment is performed using a power density of approximately 0.65 W/cm^2 for InAs/(In,Al,Ga)As and of approximately 2.6 W/cm^2 for InAs/(In,Al)As QDashes.

InAs, ignoring the intermixing at interfaces and the possible quasicontinuous change of the effective WL thickness. We approximate the energy of the WL transition by the difference between the electron and hole ground states and we plot it in Fig. 4(a). We mark the WL absorption edge estimated from the $\Delta R/R$ signal (Table II) using horizontal lines. Assuming that the WL thickness varies by InAs monolayers (1ML ≈ 0.3 nm), we establish that in both cases, the WL thickness is 3 MLs (approximately 0.9 nm). This finding is in agreement with TEM studies of similar structures [65] and with previous estimations of the WL thickness for InAs/(In,Al,Ga)As QDashes [67], as well as for InAs/InP QDs [68].

Taking the WL thicknesses of 0.9 nm for both material systems, we calculate the electronic structure of a QDash on the WL. We assume a semiellipsoid shape and we take height $H = 2.4$ nm (from the WL top edge to the top of a QDash), base width $W = 14.4$ nm, and length $L = 40$ nm, as this geometry explains the observed QDash PL energies in both cases well. The modeling of QDashes is described in detail in Sec. IV A, where the choice of such dimensions
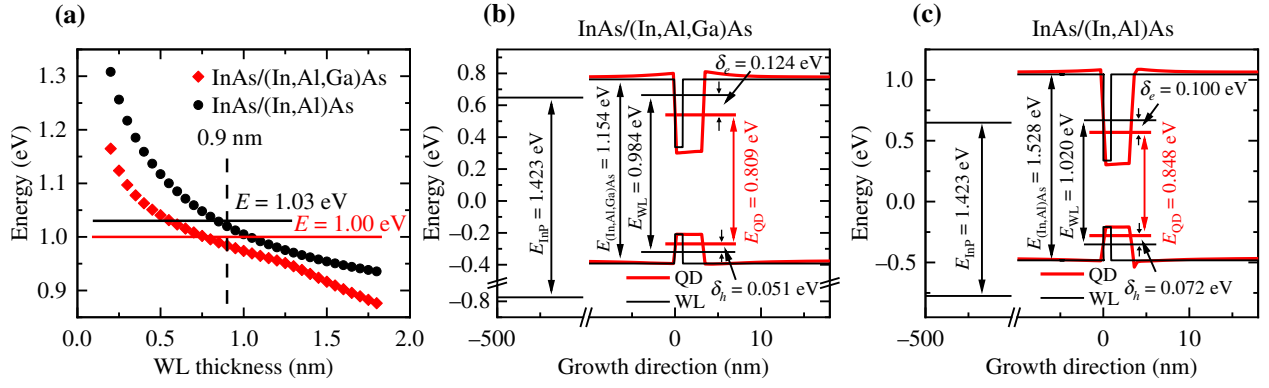
FIG. 4. Calculations of the band structure within the eight-band $\mathbf{k} \cdot \mathbf{p}$ method. (a) The ground-state energy of the WL as a function of the InAs WL thickness. The horizontal lines correspond to the WL absorption edges extracted from the PLE signal and the $\Delta R/R$ traces. (b),(c) Band diagrams for the WL (black lines) and QDashes on the WL (red lines) with marked carrier ground-state levels for the (b) InAs/(In,Al,Ga)As and (c) InAs/(In,Al)As systems. Zero on the vertical axis corresponds to a WL or QDash bottom edge.

is justified. Figures 4(b) and 4(c) show the band structures of simulated QDashes (embedded in the barrier material, red lines) and of the 0.9 nm-thick WL (surrounded by barriers and InP, black lines) for the InAs/(In,Al,Ga)As [Fig. 4(b)] and InAs/(In,Al)As [Fig. 4(c)] systems. We also calculate the energy differences between the conduction- and valence-band edges for the barriers and InP and compare them with experimental values in Table II. The uncertainties in the parameters are determined by the experimental technique used. For E_{QDash}, known from PL experiment, the uncertainty is approximately 1 meV, while for all other energies, the accuracy is lower (estimated to be 20 meV), as they are obtained solely from PLE and $\Delta R/R$ absorption experiments. The experimental and calculated values agree very well within the experimental uncertainties (the slight discrepancy in the E_{QDash} values originates from the inaccuracy of the QDash geometry estimation based on SEM images). Therefore, we can determine the energy distances for carriers between their QDash ground states and the WL continuum of states. We denote them by δ_e and δ_h for

electrons and holes, respectively, and give their values for both systems in Table III.

To compare these values with respective $E_{a,1}$ activation energies, we need to account for electron-hole Coulomb interaction $\Delta_C \sim 10$ meV, as the exciton binding needs to be broken for one of the carriers to escape. Bearing this in mind, we note that for InAs/(In,Al,Ga)As QDashes, the activation process leading to the PL quenching can be interpreted as the activation of holes from their QDash ground states to the WL continuum of states, as $\delta_h = 51$ meV together with Δ_C are close to the experimental value of $E_{a,1} \approx 50$–60 meV. We need to note here that this does not exclude the escape of electrons (characterized by twice larger activation energy $\delta_e = 124$ meV). Unless it is much stronger, such a process is imperceptible compared to the lower-energy one, as its presence only manifests itself at high temperatures, where the signal is too weak. Subsequently, carriers activated to the WL relax nonradiatively (via carrier-phonon interaction). They can be either redistributed between QDashes, as we show later, or trapped by structural defects, and do not contribute to the PL intensity. For InAs/(In,Al)As QDashes, we have $E_{a,1} = 110 \pm 20$ meV, which fits the theoretical value for the escape of electrons, $\delta_e = 100$ meV plus Δ_C. However, we have to consider the substantial fitting uncertainty and the fact that for these QDashes, δ_h is relatively close to δ_e. Two processes with such similar energies may be impossible to separate in the fitting. Thus, most probably, activation of both carrier types coexists, with electron escape being dominant, which is reflected in the observed $E_{a,1}$ value. This seems unusual since, given that $\delta_h < \delta_e$, it should be easier to excite a hole. However, the time scales of subsequent dynamics within WL, relaxation, and trapping in a QDash also play a role here. If these are faster for electrons, they have more free states available to be excited to or from a QDash, which may explain the observed result.

TABLE III. A summary of the PL quenching parameters for both QDash structures and the calculated energy distances between the QDash and WL ground states.

| Parameter | InAs/(In,Al,Ga)As | | InAs/(In,Al)As |
	Nonresonant	Quasiresonant	Quasiresonant
$E_{a,1}$	59 ± 11 meV	50.0 ± 7.7 meV	110 ± 20 meV
B_1	(10.6 ± 0.5)	(14.2 ± 0.7)	(13.3 ± 0.6)
	$\times 10^3$	$\times 10^3$	$\times 10^3$
$E_{a,2}$	9.6 ± 2.3 meV	5.6 ± 2.2 meV	19.9 ± 1.3 meV
B_2	3.4 ± 0.4	1.4 ± 0.2	8.1 ± 0.6
δ_e (Calc.)	124 meV		100 meV
δ_h (Calc.)	51 meV		72 meV

Considering calculated electronic structures, the second activation process with activation energies $E_{a,2} \approx 5 - 9$ meV and $E_{a,2} \approx 20$ meV, respectively, cannot be related to excitation to the WL. The calculated energy difference between the first excited hole state for InAs/(In,Al,Ga)As QDash and the ground state is 7.5 meV (with a few millielectronvolts variation depending on geometry) which is in good agreement with the energy $E_{a,2}$. The analogous difference for electron states is 19.0 meV. Therefore, we can ascribe the $E_{a,2}$ activation energy to the activation of holes from their QDash ground states to the first excited states. On the other hand, corresponding energy differences for InAs/(In,Al)As QDashes are 8.4 meV for holes and 20.3 meV for electrons. The value $E_{a,2} \approx 20$ meV is twice as large as the hole level splitting but it fits very well to the value calculated for the electron. However, it seems unexpected that the PL intensity is affected more by the promotion of carriers with higher activation energies. It is thus not straightforward to determine the specific process responsible for the PL quenching. Similar activation energies in the range of 20–25 meV have been observed for three structures with a varying nominal thickness of the InAs/(In,Al)As QDash layer in Ref. [59]. The associated activation process has been attributed to the activation of carriers to their excited QDash states and subsequent DS coupling (thermally assisted redistribution of carriers from small to large QDashes). Following this interpretation, we conjecture that dissipative redistribution via DS coupling is more robust for electrons, most probably due to stronger phonon coupling.

Here, the amplitudes B_1 and B_2 are very different, varying by 4 orders of magnitude in both material systems. Therefore, the second activation process is much weaker than the first and, as a result, it is of minor importance for the interpretation of the experimental data. However, in principle, we cannot exclude the presence of DS coupling between QDashes for the two material systems. Such a process would start with the promotion of carriers to excited states that are in turn coupled to states confined in adjacent QDashes, as in Ref. [59]. Many processes can be involved in the formation of DS coupling. This coupling should be manifested in narrowing the PL peak at moderate temperatures, which is considered to be its fingerprint [41,42,54]. However, this is not the case for the studied structures, as neither in Fig. 3(c) nor in Fig. 3(f) is an additional narrowing observable. Here, the only narrowing that is present stems from the WL-assisted redistribution of carriers.

The different widths of the emission from InAs/(In,Al)As QDashes under non- and quasiresonant excitation schemes may be connected with different occupations of QDashes at low temperatures, as the PL broadening reaches similar values of approximately 70 meV at high temperatures.

Finally, the peak emission energies are compared with the trends expected from the Varshni relation [dashed lines in Figs. 3(b) and 3(e)] [69]:

$$E_g(T) = E_g(0) - \frac{\alpha T^2}{T + \beta}, \qquad (2)$$

where E_g is the band-gap energy and we adopt the following parameters for InAs: $\alpha = 2.76 \times 10^{-4}$ eV^2 and $\beta = 93$ K. As the formula takes into account only the thermal change of the semiconductor band gap, any additional effects exhibit as deviations from this trend. A pronounced deviation is observable in the same temperature range as the narrowing of the PL width: both are seen, at $T \approx 35$ K for InAs/(In,Al,Ga)As and $T \approx 75$ K for InAs/(In,Al)As QDashes. Therefore, we connect these observations with the activation of carriers to the WL and their subsequent redistribution, constituting the CS coupling. It is manifested in the emission of the high-energy tail of the QDash ensemble, which is inactive at low temperatures and under weak excitation.

To sum up the results of the temperature-dependent studies, we find that for both material systems, the quenching of the PL emission is characterized by two activation processes. We connect the higher-energy one with the excitation of carriers [mainly holes for InAs/(In,Al,Ga)As and electrons for InAs/(In,Al)As] to WL states. Part of the carriers is redistributed back among the QDash ensemble (CS coupling of QDashes), which causes the observed PL narrowing and deviation from the Varshni relation. Some of the carriers are lost in the WL. The lower-energy activation process is much weaker and most probably connected with activation of the carriers to their excited states in QDashes. Excited exciton states in QDashes typically have lower oscillator strength [29], which effectively decreases the PL intensity. Carriers in such excited states could couple within the DS mechanism. However, we do not observe an additional characteristic PL narrowing to support this possibility. Finally, in Fig. 3, we mark with the shaded areas the low-temperature ranges, which we define as the temperatures for which, roughly, the PL intensity and peak width stay unchanged and the PL energy follows the Varshni trend. The ranges are $T < 25$ K for InAs/(In,Al,Ga)As and $T < 35$ K for InAs/(In,Al)As QDashes.

D. Time-resolved PL

The TRPL measurements are performed at $T = 4.2$ K to evaluate the presence of direct interdash coupling in both structures. The low-temperature condition excludes both the CS and DS coupling, with their signatures expected to lie well outside the shaded area in Fig. 3. Moreover, the excitation power is sufficiently low to exclude the impact of excited states (3.5 W/cm^2), even though no signs of

their emission are seen even at high powers [see Figs. 2(c) and 2(d)]. Therefore, it is safe to assume that the TRPL experiment largely probes the ground-state transition in QDashes.

The TRPL is recorded at various emission energies across the PL band to probe the emission dynamics for different QDash subensembles (Fig. 5). To take into account the two-component character of decays and the varying signal rise time, we fit TRPL traces with

$$I(t) = \int_0^t dt' \dot{X}(t') \, D(t - t'), \qquad (3)$$

where $D(t) = A_1 \exp(-t/\tau_{D,1}) + A_2 \exp(-t/\tau_{D,2})$ is the two-component exponential decay convoluted with the effective pumping rate of the exciton ground-state occupation $X(t)$. The latter is obtained by solving a simple set of two kinetic equations describing the pumping of some

auxiliary excited state with a Gaussian pulse and subsequent relaxation to the ground state, which is responsible for the variable rise time of the signal. We subtract the constant level of background counts from the registered time trace and fit Eq. (3) to the TRPL data using the standard method of least squares.

We plot the normalized time traces in Figs. 5(a) and 5(b), stacked for easier comparison, and find a single rise time, τ_R [see Fig. 5(b)] and two decay times, $\tau_{D,1}$ and $\tau_{D,2}$ [Fig. 5(a)]. The extracted PL decay times are compared in Fig. 5(c), while the rise times are plotted in Fig. 5(d). In both panels, these time constants are presented on top of steady-state PL emission bands to highlight possible correlations. The figures show a pronounced difference in the spectral dependencies of the decay and rise times between the two structures. First, for the InAs/(In,Al)As QDashes, there is no clear dispersion of the PL decay times, with $\tau_{D,1} \approx 1.2$–1.3 ns and $\tau_{D,1} \approx 5$–6 ns. Second,
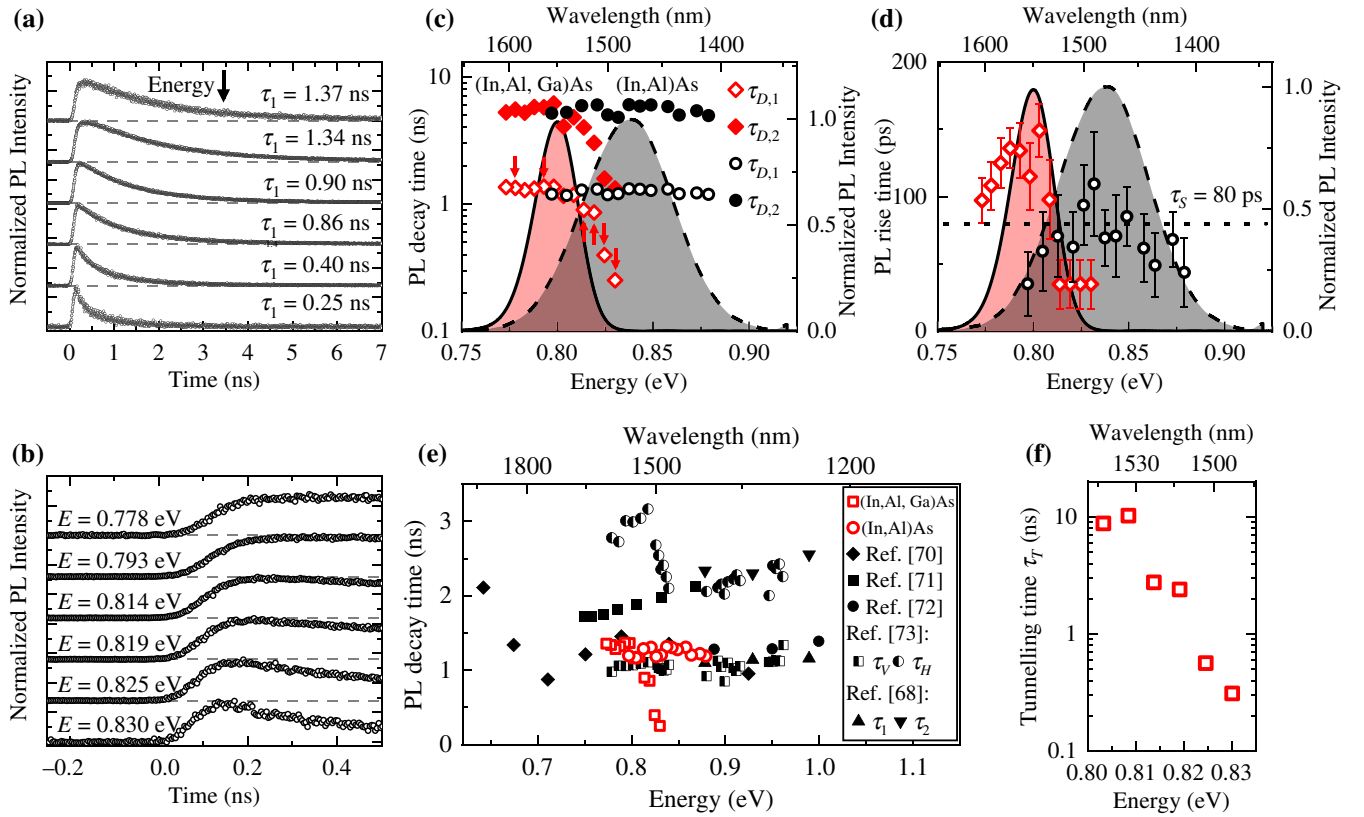
FIG. 5. Time-resolved PL. (a) Normalized time-resolved PL curves (linear scale) recorded at a low-excitation power density of 3.5 W/cm², at energies indicated by the arrows in (c). (b) An enlargement of (a), showing the rise of the TRPL signal. The curves in panels (a) and (b) are stacked for easier comparison. (c) The PL decay times $\tau_{D,1}$ and $\tau_{D,2}$. (d) The PL rise times τ_R for InAs/(In,Al,Ga)As (diamonds) and InAs/(In,Al)As QDashes (circles) with low-temperature PL spectra (solid line, InAs/(In,Al,Ga)As QDashes; dashed line, InAs/(In,Al)As QDashes). The dashed line in (d) at $\tau_S = 80$ ps marks the temporal resolution of our TRPL setup. The error bars in (d) reflect the τ_R fitting accuracy, while the bars in (c) are smaller than the symbol size and as such not visible. (e) A comparison of the measured decay times with the literature data: $\tau_{D,1}$ times for InAs/(In,Al,Ga)As QDashes (red squares) and InAs/(In,Al)As (red circles). The black full and semifull symbols show the literature data for similar InP-based ensembles of QDs or QDashes: diamonds, Ref. [70]; squares, Ref. [71]; circles, Ref. [72]; semifull squares, τ_V in Ref. [73]; semifull circles, τ_H in Ref. [73]; triangles, Ref. [68] (two-component exponential decay). (f) The tunneling times τ_T calculated according to Eq. (4).

there is no spectral dependence of the rise time with values oscillating around the setup temporal resolution $\tau_S \approx$ 80 ps, represented by the dashed black line in Fig. 5(d). Conversely, for the InAs/(In,Al,Ga)As QDashes, the PL decay times exhibit a strong dispersion across the PL band, which decreases rapidly with an increasing emission energy. Moreover, it correlates with the dispersion of the PL rise times, with τ_R clearly larger than τ_S for the low end of the band (with a peak of $\tau_R \approx 150$ ps near the PL peak center of mass) and fit results falling below τ_S for the high end. Although the uncertainties of the TRPL curve-fitting procedure are considerable, the qualitative change between the rise times at the low- and high-energy tails of the PL band can be observed directly in the traces presented in Fig. 5(b).

Let us discuss the PL lifetime of InAs/(In,Al)As QDashes first. In Fig. 5(e), we show the shorter time, $\tau_{D,1}$, superposed on a background of results from the literature. It is within the range of experimental values for InAs/InP QDs and QDashes [26,68,72,73] and close to the theoretical values for the exciton radiative lifetime along with a characteristic nearly flat dispersion [68,71,73]. Therefore, one can interpret $\tau_{D,1}$ for InAs/(In,Al)As QDashes as the radiative lifetime of excitons confined in the QDash ground state. Since the confinement is similar in both QDash systems, as shown by the calculations, we expect comparable properties of the exciton radiative lifetime in InAs/(In,Al,Ga)As and InAs/(In,Al)As QDashes. This is confirmed by the extracted $\tau_{D,1}$ values for InAs/(In,Al,Ga)As QDashes in the low- to medium-energy range. Here, the PL decay times are similar to those of InAs/(In,Al)As QDashes. Unexpectedly, the PL decay times for InAs/(In,Al,Ga)As QDashes decrease abruptly for the emission energy above the PL peak center of mass. This suggests that for this spectral range, some nonradiative or carrier-transfer processes occur. Assuming a single process of this type, its contribution to the extracted PL decay time τ_{PL} is

$$\frac{1}{\tau_{PL}} = \frac{1}{\tau_{rad}} + \frac{1}{\tau_T}, \tag{4}$$

where τ_{rad} is the radiative lifetime and τ_T is the characteristic time of the additional process. As a result, most probably τ_{rad} is nearly emission-energy independent, as discussed previously, but τ_T has a strong dispersion. We state a tentative hypothesis in which τ_T describes the interdash direct coupling supporting carrier-transfer phenomena from higher- to lower-energy states confined in adjacent InAs/(In,Al,Ga)As QDashes. Such a process should lead to both observed features: a decrease of the observed PL lifetime in high-energy QDs that lose carriers and an extension of the PL buildup time in low-energy QDs that gain them, provided that both types of carriers are transferred.

The lateral coupling between QDs has been studied in dense ensembles (QD superlattices) of epitaxial GaAs-based QDs, showing a mobility edge [47,48]. In QD chains [46,57,58,74], the direct coupling is an indication of a quantum-wire-like character of confinement [57]. A direct coupling in the form of Förster energy transfer has been studied in monodisperse CdSe nanocrystal QDs [75]. However, according to the literature, such a coupling has not been observed for the investigated InAs/(In,Al,Ga)As QDashes.

In previous theoretical works, the direct coupling between electron states, and their transfer between adjacent InAs/(In,Al,Ga)As QDashes, has been considered [49,60], although hole migration is also possible. In the TRPL experiment, we cannot distinguish between the electron or hole transfer. Most probably, both occur at possibly unequal rates. Thus, in our further theoretical considerations we evaluate the strength of direct coupling for both types of carriers, while from the experiment we may extract only a single effective value indicating carrier migration. The strong dispersion of τ_{PL}, manifested in the high-energy tail of the PL band, suggests that the transfer occurs from the ground state of a high-energy QDash to a ground or excited state of an adjacent larger one. The proposed coupling mechanism is different from the Förster energy transfer caused by the incoherent long-range dipolar interaction [75] or from the coupling via minibands formed in regular QD superlattices [47,48,54].

Thus, we identify the nonradiative process observed for high-energy InAs/(In,Al,Ga)As QDashes as a charge transfer. Equation (4) allows for the estimation of the effective carrier-transfer time τ_T. For this, τ_{PL} is the extracted PL lifetime and for τ_{rad}, we use the nearly energy-independent radiative recombination time estimated by averaging $\tau_{D,1}$ over the nondispersive range of energy values. Calculated charge transfer times are presented in Fig. 5(f); τ_T increases significantly with a decreasing emission energy.

The dispersion of the PL rise times for the InAs/(In,Al,Ga)As QDashes presented in Fig. 5(d) is more puzzling. For InAs/InP QDs or QDashes, one could expect the carrier relaxation to the ground state to occur in 8–40 ps [25,76]. Despite the temporal resolution of the TRPL setup, the rise time is substantially longer, indicating either a delayed carrier capture process or slow relaxation among QDash confined states. Since τ_R dispersion seems to be correlated with the dispersion of the decay time, the slow QDash ground-state feeding process can be related to a slow carrier transfer between adjacent QDashes. A similar relaxation bottleneck has been observed for the InAs/(In,Al,Ga)As QDs coupled to an (In,Al)As quantum well through a thin (In,Al,Ga)As barrier [76]. The relaxation bottleneck has been attributed to the weak coupling of carriers to phonons caused either by a specific transition energy or differing symmetry of the carrier states involved. The interdash charge transfer mechanism discussed here

for InAs/(In,Al,Ga)As QDashes is also phonon mediated and we may be dealing with a similar bottleneck.

The last unresolved issue is related to $\tau_{D,2}$. Four-wave mixing experiments suggest the presence of the two-exponential decays in InAs/(In,Al,Ga)As/InP QDashes [77,78] that have been attributed to strain [78]. Such two-component decays have indeed been observed [26,73] and have been explained by light-hole admixture to the nominally heavy-hole excitons, resulting from the QDash asymmetry. However, the long-time components in these reports are $\tau_H = 1.4 \pm 0.1$ ns [26] and $\tau_H < 3.5$ ns [73], much shorter than observed here. Thus, the origin of the $\tau_{D,2}$ decay component is unknown and requires further investigation.

IV. CALCULATIONS

We perform extensive theoretical modeling of the QDash electronic structure, utilizing the eight-band $\boldsymbol{k}\cdot\boldsymbol{p}$ method to show the possibility of direct interdash carrier tunneling. As already stated, we adopt a WL thickness of 0.9 nm (3 MLs) in both cases. For calculations of the electronic structure, we take the geometry of a lens-shaped (semiellipsoid) QDash, with the base width-to-height ratio of $W/H = 6$, which we keep fixed for all QDashes, according to Ref. [79].

A. Single-QDash modeling

We change the QDash height in steps of 1 ML in the range of 1.2–3.6 nm, adjusting the width proportionally. We keep the length equal to the determined median value of $L = 40$ nm. Figure 6(a) presents the calculated transition energies as a function of QDash height for the InAs/(In,Al,Ga)As and InAs/(In,Al)As systems. The shaded areas correspond to the observed emission energies: the boxes are centered at the PL peak-emission energy at low temperature and their heights are equal to the full width at half maximum (FWHM) of the PL peaks (27 meV and 55 meV, for InAs/(In,Al,Ga)As and InAs/(In,Al)As QDashes, respectively). Based on this, we can trace back the ranges of QDash widths that correspond to central parts of the respective emission peaks: 14.1–16.4 nm and 13.1–16.9 nm, for InAs/(In,Al,Ga)As and InAs/(In,Al)As QDashes, respectively, as marked by dashed lines in Fig. 6(a). We also estimate the impact of the QDash length in the range of $L = 20$–60 nm on the transition energy for selected QDash heights. The results are plotted in Fig. 6(a) using triangles and diamonds. As expected, varying the QDash length changes the emission energy by only a few millielectronvolts, which is irrelevant for this study.

It is interesting to compare calculated geometries of QDashes with their actual size distributions. Here, we focus on the width, which is more accurately determined than the height. Figure 6(b) presents histograms of QDash

widths together with normal distributions that correspond to the calculated width ranges. At this point, we translate the QDash base width into the width taken at 50% of its height [as defined in Fig. 1(c)] by simple geometrical considerations and we shift calculated Gaussian profiles in Fig. 6(b) accordingly. For both QDash ensembles, we obtain good agreement concerning the median width values, 15 nm for InAs/(In,Al,Ga)As QDashes and 16 nm for InAs/(In,Al)As ones. In the latter case, the tails of the determined and calculated distributions for low W values agree with each other, while there are more large QDashes ($W > 20$ nm) than predicted by the calculation. They possibly remain optically inactive because of structural defects in large QDashes due to the onset of strain relaxation, resulting in dislocations [80].

A similar observation can be made for large InAs/(In,Al,Ga)As QDashes. Interestingly, in their case, a significant discrepancy is also present at the low-W end of the statistics. Thus, many small QDashes from the ensemble do not contribute to the PL, possibly due to efficient out-tunneling of carriers. This observation, which is absent for InAs/(In,Al)As QDashes, can be seen as a manifestation of the direct coupling in the InAs/(In,Al,Ga)As ensemble.

B. Tunnel coupling in QDash pairs

On the basis of the calculated emission energies for single QDashes [Fig. 6(a)], for further calculation we assume that for both QDash ensembles, the high- and low-energy parts of the spectrum can be approximately represented by two QDash models: $H = 2.4$ nm and $W = 14.4$ nm (low dash, LD) and $H = 2.7$ nm, $W = 16.2$ nm (high dash, HD). With these geometries, the observed interdash direct coupling may be explained as carrier tunneling from the ground state in a LD into the ground state or any of the excited states of a HD. However, we need to check whether this is feasible and whether there really is an expected
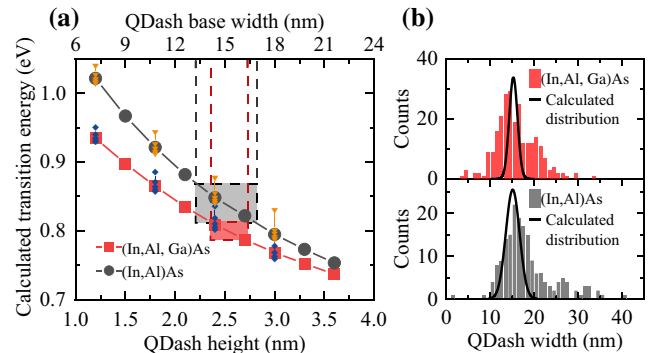
FIG. 6. (a) The calculated transition energies for InAs/(In,Al,Ga)As and InAs/(In,Al)As QDashes as a function of the QDash height. The shaded areas correspond to the PL peak energies. (b) A comparison of the observed QDash width distribution and the calculated QDash widths.

difference in its probability between the two considered material systems.

To this end, we model identical pairs formed by LDs and HDs separated by a distance d in both the InAs/(In,Al)As and InAs/(In,Al,Ga)As material systems. The strength of the tunnel coupling t may be revealed by the width of an anticrossing of energy levels in the two QDashes as the carrier is pushed from one to the other using an electric field directed along their displacement [81]. Assuming no coupling to other levels, the two states localized in different QDashes and subject to the electric field $\mathcal{E} \parallel \boldsymbol{d}$ are described by the Hamiltonian

$$H(\mathcal{E}) = \begin{pmatrix} -\frac{\Delta}{2} + \alpha\mathcal{E} & t \\ t & \frac{\Delta}{2} - \alpha\mathcal{E} \end{pmatrix}, \qquad (5)$$

where Δ is the splitting of levels without the field and α is the proportionality constant, including fundamental and material constants as well as QDash separation. At resonance, i.e., when $\alpha\mathcal{E} = \Delta/2$, the splitting of levels is minimal and equal to $2t$, which allows the determination of t from this anticrossing width. We utilize this in the theoretical calculation to evaluate the strength of direct coupling for carriers. Note that in our calculation, the electric field is just an auxiliary theoretical parameter to drive the two energy levels to resonance and read the minimal splitting. The tunnel coupling t leads to the mixing of states in two QDashes, the size of which is approximately t/Δ for $t \ll \Delta$ without any external field. In Fig. 7, we show the calculated six lowest-energy levels for the electron (top) and the hole (bottom) in a double QDash with $d = 6$ nm as a function of the electric field. The left-hand panels show the results for the InAs/(In,Al)As system and the right-hand panels for the InAs/(In,Al,Ga)As one. The dashed vertical lines mark the positions of the main anticrossings, where same-shell tunnel couplings are revealed. Let us begin by noting that for holes, the width of these tunnel resonances is similar. On the other hand, we deal with a significant difference in tunnel couplings for electrons. As expected, on the basis of our experimental results, in the InAs/(In,Al,Ga)As system, we deal with significantly stronger coupling. Apart from main resonances, we may evaluate the strength of the s-p shell tunnel couplings marked with arrows on one side of each spectrum. For now, we deal with an aligned double QDash, i.e., the dash centers lie on one line. Thus, nominally, the tunnel coupling for states of different parity (along a QDash) is forbidden. This is the case for the electron, where no splitting is present for InAs/(In,Al)As QDashes and a very small amount of splitting for the InAs/(In,Al,Ga)As system. However, for the hole, we deal with significant anticrossings caused by subband mixing due to strain and spin-orbit effects. These are slightly more pronounced in the InAs/(In,Al,Ga)As system.

From these results, we may judge that at identical QDash separations, the overall tunneling probability is significantly larger in the InAs/(In,Al,Ga)As system. While the same-shell tunnel coupling for holes is similar in both systems, that for s-p is much stronger, which also applies to the same-shell coupling for electrons. Most importantly, for the transfer of luminescence from the high-energy end of the PL spectrum to the low-energy one, both carrier types have to tunnel efficiently. This condition holds for the InAs/(In,Al,Ga)As system only, while for InAs/(In,Al)As QDashes, we deal mainly with the possibility of hole tunneling.

Next, we repeat the above calculation for d varying from 2 to 12 nm. From each spectrum, we extract the s and p same-shell anticrossing widths and hence t, which are presented in Fig. 8 as a function of the distance d. Using two types of symbols, we compare the values for the two material systems. The results for the s (left-hand panels) and p (right-hand panels) shells are similar. At the top, we see that the difference in the electron-tunnel coupling between the two material systems increases with d. For holes, the values are similar over the entire range, with stronger decay with d in the case of InAs/(In,Al)As QDashes.
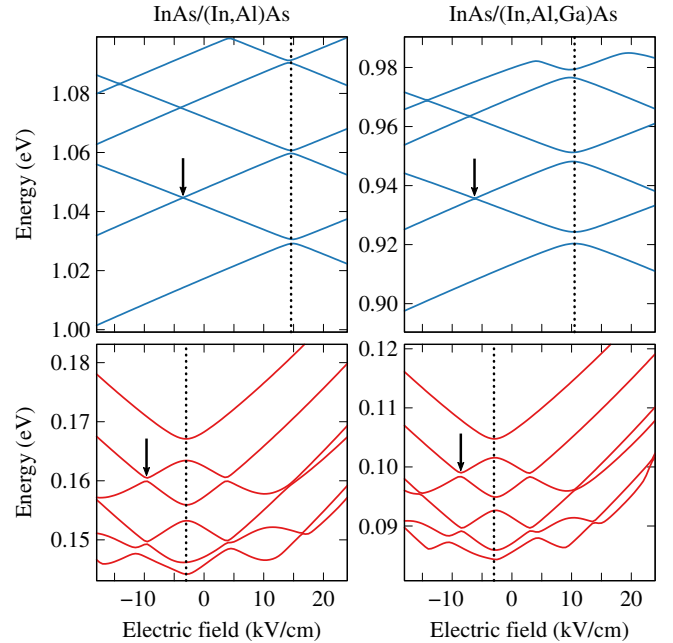
FIG. 7. The calculated energy of the six lowest conduction (top panels) and valence (bottom panels) states for a pair of InAs/(In,Al)As (left-hand panels) and InAs/(In,Al,Ga)As (right-hand panels) QDashes with $d = 6$ nm, as a function of the in-plane electric field. The energy-axis units are common for the left- and right-hand panels. The vertical dotted lines mark the main same-shell tunnel anticrossings, while the arrows mark s-p ones on one side of each spectrum.
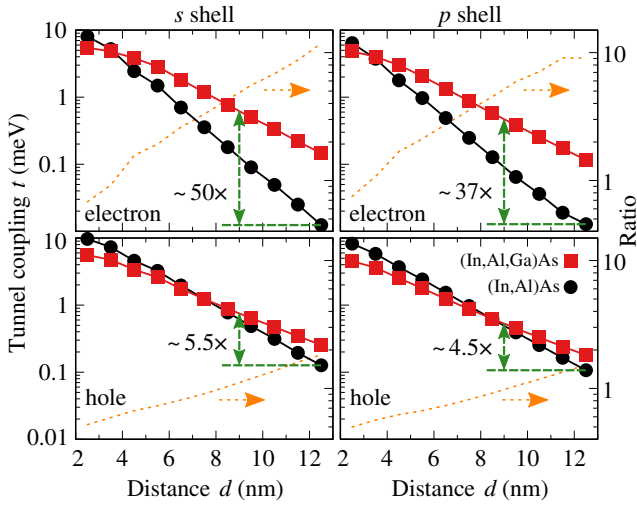
FIG. 8. The calculated tunnel coupling for electrons (top panels) and holes (bottom panels) in orbital s (left-hand panels) and p (right-hand panels) shells for InAs/(In,Al)As (circles) and InAs/(In,Al,Ga)As (squares) QDashes as a function of the distance d. The dotted lines associated with the right-hand axes show the ratio of values for the InAs/(In,Al,Ga)As and InAs/(In,Al)As systems.

In addition to comparing the values at equal distances, we need to make a comparison conforming to the actual samples that we investigate experimentally. On the plots in Fig. 8, we mark the differences between tunnel couplings at $d = 9$ nm for the InAs/(In,Al,Ga)As system and $d = 12.5$ nm for the InAs/(In,Al)As system, which reflects the average morphological data. While even at equal distance, carrier tunneling is less probable in the InAs/(In,Al)As system, the slightly larger separation of QDashes makes them much more isolated, with significantly weaker coupling for both carrier types than for InAs/(In,Al,Ga)As QDashes.

In reality, QDashes are never ideally aligned, so we perform another series of calculations for a pair with a misalignment (a difference in the positions of the centers in the elongation direction) varying up to $L/2$ while keeping $d = 6$ nm fixed. In Fig. 9, we show the widths of the different-shell (s-p) anticrossings for both carrier types. Again, we use two types of symbols to show results for InAs/(In,Al)As and InAs/(In,Al,Ga)As QDashes. As the symmetry is broken, we observe an initial abrupt appearance (for electrons) and enhancement (for holes) of the s-p coupling. Then, at approximately $L/4$, all dependencies have maxima and the couplings become weaker when the displacement is increased further. This reversal of trends results from the increasing separation of the QDash centers. Over the whole range of displacements, we observe similar results as previously: comparable coupling for holes and a much stronger coupling for electrons in the InAs/(In,Al,Ga)As system.
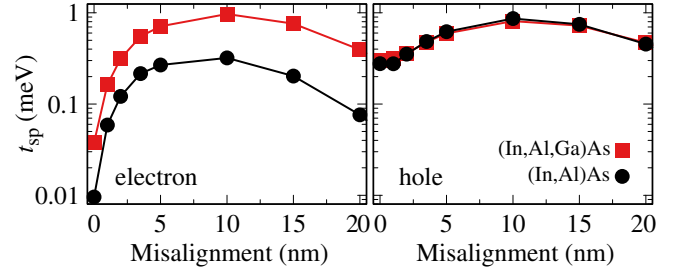
FIG. 9. The calculated s-p shell tunnel coupling for electrons (left-hand panel) and holes (right-hand panel) for InAs/(In,Al)As (circles) and InAs/(In,Al,Ga)As (squares) QDashes as a function of their misalignment along the elongation axis.

The results of modeling the QDash pairs confirm that the interdash coupling is much more probable in the case of InAs/(In,Al,Ga)As QDashes, which is in agreement with our TRPL data. In particular, only the InAs/(In,Al,Ga)As system allows for tunneling of both electrons and holes, which is needed for the transfer of luminescence.

V. SUMMARY AND CONCLUSIONS

In conclusion, we compare systems of InAs/(In,Al,Ga)As/InP and InAs/(In,Al)As/InP QDashes emitting at the telecommunication-relevant range around 1.55 μm in systematic optical studies and model their electronic structure within the multiband $\boldsymbol{k} \cdot \boldsymbol{p}$ approach. We focus on the isolation of emitters and identify the direct (tunnel) and indirect (excitation) channels of coupling and evaluate their strength in each type of QDash. On the basis of analysis of the SEM images, we establish that the QDash widths and interdash distances in the two QDash ensembles are comparable. In the results of temperature-dependent PL, we observe the redistribution of carriers among QDashes via WL states for both systems, which is an additional indirect channel of interdash coupling at elevated temperatures. Most importantly, in the case of InAs/(In,Al,Ga)As QDashes, we obtain an indication of direct interdash coupling at low temperature, as we observe a substantial dispersion of decay and rise times for the PL signal in the time-resolved PL experiment. We interpret the decrease of decay times from 1.2–1.3 ns to approximately 250 ps as originating from carrier tunneling from high-energy QDashes into the low-energy, i.e., larger, QDashes. We show that the coupling is possible between the ground state in the high-energy QDash and a ground or excited state in the low-energy one. On the contrary, in the case of InAs/(In,Al)As QDashes, we observe comparable PL decays across the entire emission peak, with no indications of coupling. To support our interpretations, we evaluate the probability of such coupling in multiband $\boldsymbol{k} \cdot \boldsymbol{p}$ modeling of the electronic structure of neighboring QDashes. We find that the coupling probability is much higher for InAs/(In,Al,Ga)As QDashes than for

InAs/(In,Al)As ones for both carrier types in the realistic range of interdash distances. Therefore, our results indicate that the studied system of InAs/(In,Al)As QDashes offers significantly enhanced emitter isolation, which can be potentially beneficial for optoelectronic devices where the coupling causes the device performance to deteriorate, e.g., for QDash-based superluminescent diodes or photon detectors. Conversely, the InAs/(In,Al,Ga)As QDashes show the presence of quantum-mechanical coupling at a similar QDash density as for the InAs/(In,Al)As system, which can be beneficial for those optoelectronic applications where the coupling is of primary importance for the operation of the device (quantum cascade lasers, low-threshold current density lasers, or ultranarrow-line nanolasers).

ACKNOWLEDGMENTS

[1] Ł. Dusanowski, M. Syperek, P. Mrowiński, W. Rudno-Rudziński, J. Misiewicz, A. Somers, S. Höfling, M. Kamp, J. P. Reithmaier, and G. Sęk, Single photon emission at 1.55 μm from charged and neutral exciton confined in a single quantum dash, Appl. Phys. Lett. **105,** 021909 (2014).

[2] Ł. Dusanowski, M. Syperek, J. Misiewicz, A. Somers, S. Höfling, M. Kamp, J. P. Reithmaier, and G. Sęk, Single-photon emission of InAs/InP quantum dashes at 1.55 μm and temperatures up to 80 K, Appl. Phys. Lett. **108,** 163108 (2016).

[3] T. Miyazawa, K. Takemoto, Y. Nambu, S. Miki, T. Yamashita, H. Terai, M. Fujiwara, M. Sasaki, Y. Sakuma, M. Takatsu, T. Yamamoto, and Y. Arakawa, Single-photon emission at 1.5 μm from an InAs/InP quantum dot with highly suppressed multi-photon emission probabilities, Appl. Phys. Lett. **109,** 132106 (2016).

[4] T. Müller, J. Skiba-Szymanska, A. B. Krysa, J. Huwer, M. Felle, M. Anderson, R. M. Stevenson, J. Heffernan, D. A. Ritchie, and A. J. Shields, A quantum light-emitting diode for the standard telecom window around 1,550 nm, Nat. Commun. **9,** 862 (2018).

[5] M. Anderson, T. Müller, J. Huwer, J. Skiba-Szymanska, A. B. Krysa, R. M. Stevenson, J. Heffernan, D. A. Ritchie, and A. J. Shields, Quantum teleportation using highly coherent emission from telecom C-band quantum dots, npj Quantum Inf. **6,** 14 (2020).

[6] A. Musiał, P. Holewa, P. Wyborski, M. Syperek, A. Kors, J. P. Reithmaier, G. Sęk, and M. Benyoucef, High-purity triggered single-photon emission from symmetric single InAs/InP quantum dots around the telecom C-band window, Adv. Quantum Technol. **3,** 1900082 (2019).

[7] X. Cao, M. Zopf, and F. Ding, Telecom wavelength single photon sources, J. Semicond. **40,** 071901 (2019).

[8] Y. Arakawa and M. J. Holmes, Progress in quantum-dot single photon sources for quantum information technologies: A broad spectrum overview, Appl. Phys. Rev. **7,** 021309 (2020).

[9] P. Holewa, A. Sakanas, U. M. Gür, P. Mrowiński, B. Wang, K. Yvind, N. Gregersen, M. Syperek, and E. Semenova, Bright Quantum Dot Single-Photon Emitters at Telecom Bands Heterogeneously Integrated with Si (2021), ArXiv:2104.07589.

[10] P. Holewa, S. Kadkhodazadeh, M. Gawełczyk, P. Baluta, A. Musiał, V. G. Dubrovskii, M. Syperek, and E. Semenova, Droplet epitaxy symmetric InAs/InP quantum dots for quantum emission in the third telecom window: Morphology, optical and electronic properties, Nanophotonics **11,** 1515 (2022).

[11] J. Reithmaier, G. Eisenstein, and A. Forchel, InAs/InP quantum-dash lasers and amplifiers, Proc. IEEE **95,** 1779 (2007).

[12] F. Lelarge, B. Dagens, J. Renaudier, R. Brenot, A. Accard, F. van Dijk, D. Make, O. L. Gouezigou, J.-G. Provost, F. Poingt, J. Landreau, O. Drisse, E. Derouin, B. Rousseau, F. Pommereau, and G.-H. Duan, Recent advances on InAs/InP quantum dash based semiconductor lasers and optical amplifiers operating at 1.55 μm, IEEE J. Sel. Top. Quantum Electron. **13,** 111 (2007).

[13] M. Z. M. Khan, T. K. Ng, and B. S. Ooi, Self-assembled InAs/InP quantum dots and quantum dashes: Material structures and devices, Prog. Quantum Electron. **38,** 237 (2014).

[14] N. Wingreen and C. Stafford, Quantum-dot cascade laser: Proposal for an ultralow-threshold semiconductor laser, IEEE J. Quantum Electron. **33,** 1170 (1997).

[15] A. Lyakh, R. Maulini, A. Tsekoun, R. Go, C. Pflügl, L. Diehl, Q. J. Wang, F. Capasso, and C. K. N. Patel, 3 W continuous-wave room temperature single-facet emission from quantum cascade lasers based on nonresonant extraction design approach, Appl. Phys. Lett. **95,** 141113 (2009).

[16] V. Liverini, A. Bismuto, L. Nevou, M. Beck, and J. Faist, Midinfrared electroluminescence from InAs/InP quantum dashes, Appl. Phys. Lett. **97,** 221109 (2010).

[17] V. Liverini, L. Nevou, F. Castellano, A. Bismuto, M. Beck, F. Gramm, and J. Faist, Room-temperature transverse-electric polarized intersubband electroluminescence from InAs/AlInAs quantum dashes, Appl. Phys. Lett. **101,** 261113 (2012).

[18] P. Martyniuk and A. Rogalski, Quantum-dot infrared photodetectors: Status and outlook, Prog. Quantum Electron. **32,** 89 (2008).

[19] J. Brault, M. Gendry, G. Grenet, G. Hollinger, J. Olivares, B. Salem, T. Benyattou, and G. Bremond, Surface effects on shape, self-organization and photoluminescence of InAs islands grown on InAlAs/InP(001), J. Appl. Phys. **92,** 506 (2002).

[20] W. Rudno-Rudziński, G. Sęk, K. Ryczko, R. Kudrawiec, J. Misiewicz, A. Somers, R. Schwertberger, J. P. Reithmaier, and A. Forchel, Optically probed wetting layer in InAs/InGaAlAs/InP quantum-dash structures, Appl. Phys. Lett. **86,** 101904 (2005).

[21] W. Rudno-Rudziński, R. Kudrawiec, P. Podemski, G. Sęk, J. Misiewicz, A. Somers, R. Schwertberger, J. P. Reithmaier, and A. Forchel, Photoreflectance-probed excited states in InAs/InGaAlAs quantum dashes grown on InP substrate, Appl. Phys. Lett. **89,** 031908 (2006).

[22] M. Gawełczyk, P. Wyborski, P. Podemski, J. P. Reithmaier, S. Höfling, and G. Sęk, Excited states of neutral and charged excitons in single strongly asymmetric InP-based nanostructures emitting in the telecom C band, Phys. Rev. B **100,** 241304(R) (2019).

[23] A. Musiał, P. Kaczmarkiewicz, G. Sęk, P. Podemski, P. Machnikowski, J. Misiewicz, S. Hein, S. Höfling, and A. Forchel, Carrier trapping and luminescence polarization in quantum dashes, Phys. Rev. B **85,** 035314 (2012).

[24] Ł. Dusanowski, M. Syperek, W. Rudno-Rudziński, P. Mrowiński, G. Sek, J. Misiewicz, A. Somers, J. P. Reithmaier, S. Höfling, and A. Forchel, Exciton and biexciton dynamics in single self-assembled InAs/InGaAlAs/InP quantum dash emitting near 1.55 μm, Appl. Phys. Lett. **103,** 253113 (2013).

[25] M. Syperek, Ł. Dusanowski, J. Andrzejewski, W. Rudno-Rudziński, G. Sęk, J. Misiewicz, and F. Lelarge, Carrier relaxation dynamics in InAs/GaInAsP/InP(001) quantum dashes emitting near 1.55 μm, Appl. Phys. Lett. **103,** 083104 (2013).

[26] M. Syperek, K. Ryczko, M. Dallner, M. Dyksik, M. Motyka, M. Kamp, S. Höfling, J. Misiewicz, and G. Sęk, Room temperature carrier kinetics in the W-type GaInAsSb/InAs/AlSb quantum well structure emitting in mid-infrared spectral range, Acta Phys. Pol. A **130,** 1224 (2016).

[27] Ł. Dusanowski, P. Mrowiński, M. Syperek, J. Misiewicz, A. Somers, S. Höfling, J. P. Reithmaier, and G. Sęk, Confinement regime in self-assembled InAs/InAlGaAs/InP quantum dashes determined from exciton and biexciton recombination kinetics, Appl. Phys. Lett. **111,** 253106 (2017).

[28] Ł. Dusanowski, M. Gawełczyk, J. Misiewicz, S. Höfling, J. P. Reithmaier, and G. Sęk, Strongly temperature-dependent recombination kinetics of a negatively charged exciton in asymmetric quantum dots at 1.55μm, Appl. Phys. Lett. **113,** 043103 (2018).

[29] M. Gawełczyk, Excitons in asymmetric nanostructures: Confinement regime, Acta Phys. Pol. A **134,** 930 (2018).

[30] C. Cornet, M. Hayne, P. Caroff, C. Levallois, L. Joulaud, E. Homeyer, C. Paranthoen, J. Even, C. Labbé, H. Folliot, V. V. Moshchalkov, and S. Loualiche, Increase of charge-carrier redistribution efficiency in a laterally organized superlattice of coupled quantum dots, Phys. Rev. B **74,** 245315 (2006).

[31] N. N. Ledentsov, V. A. Shchukin, M. Grundmann, N. Kirstaedter, J. Böhrer, O. Schmidt, D. Bimberg, V. M. Ustinov, A. Y. Egorov, A. E. Zhukov, P. S. Kop'ev, S. V. Zaitsev, N. Y. Gordeev, Z. I. Alferov, A. I. Borovkov, A. O. Kosogov, S. S. Ruvimov, P. Werner, U. Gösele, and J. Heydenreich, Direct formation of vertically coupled quantum dots in Stranski-Krastanow growth, Phys. Rev. B **54,** 8743 (1996).

[32] P. Caroff, C. Paranthoen, C. Platz, O. Dehaese, H. Folliot, N. Bertru, C. Labbé, R. Piron, E. Homeyer, A. Le Corre, and S. Loualiche, High-gain and low-threshold InAs quantum-dot lasers on InP, Appl. Phys. Lett. **87,** 243107 (2005).

[33] I. C. Sandall, P. M. Smowton, H.-Y. Liu, and M. Hopkinson, Nonradiative recombination in multiple layer In(Ga)As quantum-dot lasers, IEEE J. Quantum Electron. **43,** 698 (2007).

[34] J. G. Bohnet, Z. Chen, J. M. Weiner, D. Meiser, M. J. Holland, and J. K. Thompson, A steady-state superradiant laser with less than one intracavity photon, Nature **484,** 78 (2012).

[35] F. Jahnke, C. Gies, M. Aßmann, M. Bayer, H. A. M. Leymann, A. Foerster, J. Wiersig, C. Schneider, M. Kamp, and S. Höfling, Giant photon bunching, superradiant pulse emission and excitation trapping in quantum-dot nanolasers, Nat. Commun. **7,** 11540 (2016).

[36] Z. Y. Zhang, R. A. Hogg, X. Q. Lv, and Z. G. Wang, Self-assembled quantum-dot superluminescent light-emitting diodes, Adv. Opt. Photon. **2,** 201 (2010).

[37] I. A. Dmitriev and R. A. Suris, Quantum cascade lasers based on quantum dot superlattice, Phys. Status Solidi A **202,** 987 (2005).

[38] X. L. Zhou, Y. H. Chen, J. Q. Liu, C. H. Jia, G. Y. Zhou, X. L. Ye, B. Xu, and Z. G. Wang, Temperature dependent photoluminescence of an In(Ga)As/GaAs quantum dot system with different areal density, J. Phys. D: Appl. Phys. **43,** 295401 (2010).

[39] Y. Toda, O. Moriwaki, M. Nishioka, and Y. Arakawa, Efficient Carrier Relaxation Mechanism in InGaAs/GaAs Self-Assembled Quantum Dots Based on the Existence of Continuum States, Phys. Rev. Lett. **82,** 4114 (1999).

[40] C. Kammerer, G. Cassabois, C. Voisin, C. Delalande, P. Roussignol, and J. M. Gérard, Photoluminescence Up-Conversion in Single Self-Assembled InAs/GaAs Quantum Dots, Phys. Rev. Lett. **87,** 207401 (2001).

[41] T. Mano, R. Nötzel, Q. Gong, T. v. Lippen, G. J. Hamhuis, T. J. Eijkemans, and J. H. Wolter, Temperature-dependent photoluminescence of self-assembled (In, Ga)As quantum dots on GaAs (100): Carrier redistribution through low-energy continuous states, Jpn. J. Appl. Phys. **44,** 6829 (2005).

[42] Y. I. Mazur, B. L. Liang, Z. M. Wang, G. G. Tarasov, D. Guzun, and G. J. Salamo, Development of continuum states in photoluminescence of self-assembled InGaAs/GaAs quantum dots, J. Appl. Phys. **101,** 014301 (2007).

[43] A. Vasanelli, R. Ferreira, and G. Bastard, Continuous Absorption Background and Decoherence in Quantum Dots, Phys. Rev. Lett. **89,** 216804 (2002).

[44] C. Cornet, C. Platz, P. Caroff, J. Even, C. Labbé, H. Folliot, A. L. Corre, and S. Loualiche, Approach to wetting-layer-assisted lateral coupling of InAs/InP quantum dots, Phys. Rev. B **72,** 035342 (2005).

[45] C. Cornet, A. Schliwa, J. Even, F. Doré, C. Celebi, A. Létoublon, E. Macé, C. Paranthoën, A. Simon, P. M. Koenraad, N. Bertru, D. Bimberg, and S. Loualiche, Electronic and optical properties of InAs/InP quantum dots on InP(100) and InP(311)B substrates: Theory and experiment, Phys. Rev. B **74**, 035312 (2006).

[46] V. G. Dorogan, Y. I. Mazur, E. Marega, G. G. Tarasov, M. E. Ware, and G. J. Salamo, Hybridized quantum dot-wetting layer states in photoluminescence of In(Ga)As/GaAs dot chain samples, J. Appl. Phys. **105**, 124304 (2009).

[47] S. Lan, K. Akahane, H.-Z. Song, Y. Okada, M. Kawabe, T. Nishimura, and O. Wada, Capture, relaxation, and recombination in two-dimensional quantum-dot superlattices, Phys. Rev. B **61**, 16847 (2000).

[48] S. Nishikawa, S. Lan, O. Wada, T. Nishimura, K. Akahane, and M. Kawabe, Lateral-coupling-induced modification of density of states and exciton dynamics in high-density ordered $In_{0.4}Ga_{0.6}As$/GaAs(311)B quantum dot arrays, Jpn. J. Appl. Phys. **41**, 3766 (2002).

[49] K. Ryczko, G. Sęk, and J. Misiewicz, The effect of structural parameters on the in-plane coupling between quantum dashes of a dense ensemble in the InAs-InP material system, J. Appl. Phys. **115**, 213502 (2014).

[50] M. Gong, K. Duan, C.-F. Li, R. Magri, G. A. Narvaez, and L. He, Electronic structure of self-assembled InAs/InP quantum dots: Comparison with self-assembled InAs/GaAs quantum dots, Phys. Rev. B **77**, 045326 (2008).

[51] M. Syperek, M. Baranowski, G. Sęk, J. Misiewicz, A. Löffler, S. Höfling, S. Reitzenstein, M. Kamp, and A. Forchel, Impact of wetting-layer density of states on the carrier relaxation process in low indium content self-assembled (In, Ga)As/GaAs quantum dots, Phys. Rev. B **87**, 125305 (2013).

[52] M. Bayer, P. Hawrylak, K. Hinzer, S. Fafard, M. Korkusinski, Z. R. Wasilewski, O. Stern, and A. Forchel, Coupling and entangling of quantum states in quantum dot molecules, Science **291**, 451 (2001).

[53] E. A. Stinaff, Optical signatures of coupled quantum dots, Science **311**, 636 (2006).

[54] T. v. Lippen, A. Y. Silov, and R. Nötzel, Extended electron states in lateral quantum dot molecules investigated with photoluminescence, Phys. Rev. B **75**, 115414 (2007).

[55] L. Wang, A. Rastelli, S. Kiravittaya, M. Benyoucef, and O. G. Schmidt, Self-assembled quantum dot molecules, Adv. Mater. **21**, 2601 (2009).

[56] J. Wu, X. Hu, J. Lee, E.-S. Kim, and Z. M. Wang, Epitaxially self-assemblied quantum dot pairs, Adv. Opt. Mater. **1**, 201 (2013).

[57] B. R. Wang, B. Q. Sun, Y. Ji, X. M. Dou, Z. Y. Xu, Z. M. Wang, and G. J. Salamo, Optical study of lateral carrier transfer in (In, Ga)As/GaAs quantum-dot chains, Appl. Phys. Lett. **93**, 011107 (2008).

[58] Y. I. Mazur, V. G. Dorogan, E. Marega, D. F. Cesar, V. Lopez-Richard, G. E. Marques, Z. Y. Zhuchenko, G. G. Tarasov, and G. J. Salamo, Cooperative effects in the photoluminescence of (In, Ga)As/GaAs quantum dot chain structures, Nanoscale Res. Lett. **5**, 991 (2010).

[59] N. A. Jahan, C. Hermannstädter, J.-H. Huh, H. Sasakura, T. J. Rotter, P. Ahirwar, G. Balakrishnan, K. Akahane, M. Sasaki, H. Kumano, and I. Suemune, Temperature dependent carrier dynamics in telecommunication band InAs quantum dots and dashes grown on InP substrates, J. Appl. Phys. **113**, 033506 (2013).

[60] K. Ryczko, G. Sęk, and J. Misiewicz, Lateral coupling within the ensemble of InAs/InGaAlAs/InP quantum dashes, Acta Phys. Pol. A **124**, 805 (2013).

[61] S. Birner, T. Zibold, T. Andlauer, T. Kubis, M. Sabathil, A. Trellakis, and P. Vogl, NEXTNANO: General purpose 3-D simulations, IEEE Trans. Electron Devices **54**, 2137 (2007).

[62] K. Gawarecki, P. Machnikowski, and T. Kuhn, Electron states in a double quantum dot with broken axial symmetry, Phys. Rev. B **90**, 085437 (2014).

[63] A. Mielnik-Pyszczorski, K. Gawarecki, M. Gawełczyk, and P. Machnikowski, Dominant role of the shear strain induced admixture in spin-flip processes in self-assembled quantum dots, Phys. Rev. B **97**, 245313 (2018).

[64] I. Vurgaftman, J. R. Meyer, and L. R. Ram-Mohan, Band parameters for III–V compound semiconductors and their alloys, J. Appl. Phys. **89**, 5815 (2001).

[65] G. L. Paravicini-Bagliani, V. Liverini, F. Valmorra, G. Scalari, F. Gramm, and J. Faist, Enhanced current injection from a quantum well to a quantum dash in magnetic field, New J. Phys. **16**, 083029 (2014).

[66] J. D. Lambkin, D. J. Dunstan, K. P. Homewood, L. K. Howard, and M. T. Emeny, Thermal quenching of the photoluminescence of InGaAs/GaAs and InGaAs/AlGaAs strained-layer quantum wells, Appl. Phys. Lett. **57**, 1986 (1990).

[67] R. Kudrawiec, M. Motyka, J. Misiewicz, A. Somers, R. Schwertberger, J. P. Reithmaier, A. Forchel, A. Sauerwald, T. Kümmell, and G. Bacher, Contactless electroreflectance of $InAs/In_{0.53}Ga_{0.23}Al_{0.24}As$ quantum dashes grown on InP substrate: Analysis of the wetting layer transition, J. Appl. Phys. **101**, 013507 (2007).

[68] P. Holewa, M. Gawełczyk, C. Ciostek, P. Wyborski, S. Kadkhodazadeh, E. Semenova, and M. Syperek, Optical and electronic properties of low-density InAs/InP quantum-dot-like structures designed for single-photon emitters at telecom wavelengths, Phys. Rev. B **101**, 195304 (2020).

[69] Y. Varshni, Temperature dependence of the energy gap in semiconductors, Physica **34**, 149 (1967).

[70] P. Holewa, M. Gawełczyk, A. Maryński, P. Wyborski, J. Reithmaier, G. Sęk, M. Benyoucef, and M. Syperek, Optical and Electronic Properties of Symmetric InAs/(In, Al, Ga)As/InP Quantum Dots Formed by Ripening in Molecular Beam Epitaxy: A Potential System for Broad-Range Single-Photon Telecom Emitters, Phys. Rev. Appl. **14**, 064054 (2020).

[71] M. Gong, W. Zhang, G. C. Guo, and L. He, Atomistic pseudopotential theory of optical properties of exciton complexes in InAs/InP quantum dots, Appl. Phys. Lett. **99**, 231106 (2011).

[72] S. Tomimoto, A. Kurokawa, Y. Sakuma, T. Usuki, and Y. Masumoto, Radiative recombination of excitons in disk-shaped InAs/InP quantum dots, Phys. Rev. B **76**, 205317 (2007).

[73] M. Gawełczyk, M. Syperek, A. Maryński, P. Mrowiński, Ł. Dusanowski, K. Gawarecki, J. Misiewicz, A. Somers, J. P. Reithmaier, S. Höfling, and G. Sęk, Exciton lifetime and emission polarization dispersion in strongly in-plane asymmetric nanostructures, Phys. Rev. B **96**, 245425 (2017).

[74] Y. I. Mazur, V. Lopes-Oliveira, L. D. de Souza, V. Lopez-Richard, M. D. Teodoro, V. G. Dorogan, M. Benamara, J. Wu, G. G. Tarasov, E. Marega, Z. M. Wang, G. E. Marques, and G. J. Salamo, Carrier transfer in vertically stacked quantum ring-quantum dot chains, J. Appl. Phys. **117**, 154307 (2015).

[75] S. A. Crooker, J. A. Hollingsworth, S. Tretiak, and V. I. Klimov, Spectrally Resolved Dynamics of Energy Transfer in Quantum-Dot Assemblies: Towards Engineered Energy Flows in Artificial Materials, Phys. Rev. Lett. **89**, 186802 (2002).

[76] M. Syperek, J. Andrzejewski, E. Rogowicz, J. Misiewicz, S. Bauer, V. I. Sichkovskyi, J. P. Reithmaier, and G. Sęk, Carrier relaxation bottleneck in type-II InAs/ InGaAlAs/InP(001) coupled quantum dots-quantum well

[77] W. Langbein, P. Borri, U. Woggon, V. Stavarache, D. Reuter, and A. Wieck, Radiatively limited dephasing in InAs quantum dots, Phys. Rev. B **70**, 033301 (2004).

[78] H. Tahara, Y. Ogawa, F. Minami, K. Akahane, and M. Sasaki, Anisotropic optical properties of excitons in strain-controlled InAs quantum dots, Phys. Rev. B **87**, 035304 (2013).

[79] A. Sauerwald, T. Kümmell, G. Bacher, A. Somers, R. Schwertberger, J. P. Reithmaier, and A. Forchel, Size control of InAs quantum dashes, Appl. Phys. Lett. **86**, 253112 (2005).

[80] K. Yamaguchi, in *Handbook of Nano-Optics and Nanophotonics*, edited by M. Ohtsu (Springer, Berlin, Heidelberg, 2013), p. 809.

[81] H. J. Krenner, M. Sabathil, E. C. Clark, A. Kress, D. Schuh, M. Bichler, G. Abstreiter, and J. J. Finley, Direct Observation of Controlled Coupling in an Individual Quantum Dot Molecule, Phys. Rev. Lett. **94**, 057402 (2005).

structure emitting at 1.55 μm, Appl. Phys. Lett. **112**, 221901 (2018).